

# Tracking magnetic bright point motions through the solar atmosphere

P. H. Keys,<sup>1</sup>★ M. Mathioudakis,<sup>1</sup> D. B. Jess,<sup>1</sup> S. Shelyag,<sup>1</sup> D. J. Christian<sup>2</sup> and F. P. Keenan<sup>1</sup>

<sup>1</sup>*Astrophysics Research Centre, School of Mathematics and Physics, Queen's University, Belfast, BT7 1NN*

<sup>2</sup>*Department of Physics and Astronomy, California State University, Northridge, CA 91330, USA*

Accepted 2012 October 22. Received 2012 October 15; in original form 2012 August 10

## ABSTRACT

High-cadence, multiwavelength observations and simulations are employed for the analysis of solar photospheric magnetic bright points (MBPs) in the quiet Sun. The observations were obtained with the Rapid Oscillations in the Solar Atmosphere (ROSA) imager and the Interferometric Bidimensional Spectrometer at the Dunn Solar Telescope. Our analysis reveals that photospheric MBPs have an average transverse velocity of approximately  $1 \text{ km s}^{-1}$ , whereas their chromospheric counterparts have a slightly higher average velocity of  $1.4 \text{ km s}^{-1}$ . Additionally, chromospheric MBPs were found to be around 63 per cent larger than the equivalent photospheric MBPs. These velocity values were compared with the output of numerical simulations generated using the MURAM code. The simulated results were similar, but slightly elevated, when compared to the observed data. An average velocity of  $1.3 \text{ km s}^{-1}$  was found in the simulated *G*-band images and an average of  $1.8 \text{ km s}^{-1}$  seen in the velocity domain at a height of 500 km above the continuum formation layer. Delays in the change of velocities were also analysed. Average delays of  $\sim 4 \text{ s}$  between layers of the simulated data set were established and values of  $\sim 29 \text{ s}$  observed between *G*-band and Ca II K ROSA observations. The delays in the simulations are likely to be the result of oblique granular shock waves, whereas those found in the observations are possibly the result of a semi-rigid flux tube.

**Key words:** Sun: activity – Sun: atmosphere – Sun: chromosphere – Sun: evolution – Sun: photosphere.

## 1 INTRODUCTION

Magnetic bright points (MBPs) are ubiquitous in the solar photosphere (Dunn & Zirker 1973). They are thought to be the footpoints of magnetic flux tubes in the intergranular lanes with field strengths of the order of a kilogauss (Stenflo 1985; Solanki 1993). Their brightness is due to the reduced pressure within the flux tube allowing the observer to view a deeper, hotter region of the photosphere and is also due to the heating of the plasma within the flux tube by material surrounding its walls. The higher temperature reduces the abundance of the CH molecule, making MBPs appear brighter in *G*-band (4305 Å) images (Steiner, Hauschildt & Bruls 2001; Shelyag et al. 2004). *G*-band observations therefore provide a good base for analysing the photospheric properties of these concentrated magnetic structures.

The importance of MBP studies was reviewed in de Wijn et al. (2009). Briefly, studies of MBP motions are important as these may drive Alfvén waves in magnetic field lines within flux tubes, where the energy carried by the waves can be transmitted to the

corona and lead to heating. This has been a recent topic of several three-dimensional magnetohydrodynamic (MHD) models (van Ballegoijen et al. 2011; Asgari-Targhi & van Ballegoijen 2012) investigating these effects.

Recent MBP studies have focused on their size, velocity distributions (Sánchez Almeida et al. 2004; Crockett et al. 2010; Keys et al. 2011) and intensity peaks (Langhans, Schmidt & Tritschler 2002). Bonet et al. (2008) have identified convective downdraughts and vortex motions at the location of MBPs, phenomena that have also been reproduced in simulations of radiative MHD (Shelyag et al. 2011a, b; Shelyag, Mathioudakis & Keenan 2012).

A study of MBPs in the Na I D<sub>1</sub> line (Jess et al. 2010a) has shown evidence for strong downdraughts with velocities as high as  $7 \text{ km s}^{-1}$  at MBP centres. It was also noted that field strengths affected the expansion of the flux tubes, with weak fields leading to an expansion of  $\approx 76$  per cent whereas higher field strengths led to an expansion of  $\approx 44$  per cent.

Keys et al. (2011) studied the transverse velocities of over 6000 MBPs in both observed and simulated *G*-band images. Their study revealed an average velocity of  $1 \text{ km s}^{-1}$  and a maximum value of  $7 \text{ km s}^{-1}$ . Radiative MHD simulations with an average field strengths

★ E-mail: pkeys02@qub.ac.uk

of 200 and 400 G revealed similar velocity distributions, the latter showing the best agreement with observations.

Ulmschneider, Zaehrer & Musielak (1991) have shown that the horizontal velocity of solar magnetic flux tubes increases as a function of height. The amplitude of the horizontal velocity component scales as  $\rho^{-1/2}$ , where  $\rho$  is the density, and the authors note that the transverse wave flux is only approximately conserved. In the regime of strict flux conservation, a horizontal velocity component of  $1.5 \text{ km s}^{-1}$  was expected at a height of 340 km, yet a velocity of only  $0.8 \text{ km s}^{-1}$  was observed. This is very similar to the values of Keys et al. (2011).

MBPs have average diameters of around 135 km (Sánchez Almeida et al. 2004) and lifetimes of approximately 90 s (Keys et al. 2011), and hence tracking these throughout the solar atmosphere requires high spatial and temporal resolution imaging. The accurate co-alignment of the images is vital when multiwavelength studies are considered. In this paper we use simultaneous multiwavelength observations to study MBPs at various heights in the solar atmosphere and improved MBP tracking algorithms over our previous studies (Crockett et al. 2010). We present multiwavelength observations and numerical simulations of photospheric MBPs in co-temporal and co-spatial *G*-band, Ca II K and Na I D<sub>1</sub> images. The observations and numerical simulations used are described in Section 2. Analysis of these results and their implications are presented in Section 3, with concluding remarks given in Section 4.

## 2 OBSERVATIONS AND NUMERICAL SIMULATIONS

The imaging data employed in this study were obtained using the Rapid Oscillations in the Solar Atmosphere (ROSA; Jess et al. 2010b) instrument at the Dunn Solar Telescope in New Mexico, USA. Observations were obtained during a period of excellent seeing on 2009 May 28, using a  $9.2 \text{ Å}$  wide filter centred at  $4305 \text{ Å}$  (*G*-band) and a  $1 \text{ Å}$  wide filter centred at  $3933.7 \text{ Å}$  (Ca II K core). We observed a  $69 \text{ arcsec} \times 69 \text{ arcsec}$  quiet Sun region at disc centre for  $\sim 50 \text{ min}$ , using a common plate scale of  $0.069 \text{ arcsec pixel}^{-1}$  for the ROSA cameras. The images were reconstructed using the speckle algorithm of Wöger, von der Lühe & Reardon (2008), while image destretching was performed using a  $40 \times 40$  grid (equating to an  $\approx 1.7$  separation between spatial samples; Jess et al. 2008). *G*-band images were taken at a raw cadence of  $0.033 \text{ s}$ , while after reconstruction the cadence was reduced to  $0.528 \text{ s}$ . Reconstructed *G*-band images were then binned into consecutive groups of four to improve the signal-to-noise ratio and reduce the overall volume of the data set, providing a final image cadence of  $2.1 \text{ s}$ . The Ca II K images had a raw cadence of  $0.26 \text{ s}$  and a post-speckle reconstructed cadence of  $4.2 \text{ s}$ . Subsequently, the two data sets were spatially co-aligned.

The Interferometric Bidimensional Spectrometer (IBIS; Cavallini 2006) was employed in conjunction with ROSA, covering the Na I D<sub>1</sub> absorption line at  $5895.94 \text{ Å}$ . At a spatial sampling of  $0.097 \text{ arcsec pixel}^{-1}$ , the near-square field of view (FOV) of ROSA was contained within the circular aperture of IBIS. Nine wavelength steps were utilized with IBIS, with 10 images per wavelength step to aid image reconstruction, resulting in a complete scan cadence of  $39.7 \text{ s}$ . A blueshift correction was required due to the classical etalon mountings (Cauzzi et al. 2008). Images of the Na I D<sub>1</sub> core used for MBP studies are true intensity maps, created by establishing the line-profile minimum at each pixel. By displaying Doppler-compensated line-centre intensities, rather than rest-wavelength intensities, brightness variations throughout the image

are more indicative of the source function than of the velocities present in the line formation region (Jess et al. 2010a). A sample of ROSA and IBIS images is shown in Fig. 1.

The radiative MHD code MURAM (Vögler et al. 2005) has been used to produce simulated *G*-band images and their corresponding velocity domains. This code solves large-eddy radiative three-dimensional MHD equations on a Cartesian grid and employs a fourth-order Runge–Kutta scheme to advance the numerical solution in time. The numerical domain has a physical size of  $12 \times 12 \text{ Mm}^2$  in the horizontal direction,  $1.4 \text{ Mm}$  in the vertical direction, and is resolved by  $480 \times 480 \times 100$  grid cells, respectively. Our starting point for the simulations is a well-developed non-magnetic ( $B = 0$ ) snapshot of photospheric convection taken approximately  $2000 \text{ s}$  (about eight convective turnover time-scales) from the initial plane-parallel model. A uniform magnetic field of  $200 \text{ G}$  was introduced at this stage, and a sequence of 829 snapshots recorded, each separated by a time interval of  $\sim 2 \text{ s}$ . The resulting sequence, which is used for further *G*-band radiative diagnostics, covers approximately  $30 \text{ min}$  of physical time, corresponding to  $\sim 4$ – $6$  granular lifetimes. *G*-band images were produced using the radiative diagnostic technique briefly described by Jess et al. (2012a). The plasma velocity field corresponding to these images was measured at a height of about  $500 \text{ km}$  above the continuum formation layer (see Fig. 2).

## 3 ANALYSIS AND RESULTS

Keys et al. (2011) employed an automated detection and tracking algorithm to estimate the velocities of  $6000 \text{ G}$ -band MBPs. However, an automated detection and tracking algorithm is extremely hard to employ for the Ca II K data set. Due to the reverse granulation inherent in the Ca II K images, the application of intensity thresholding for the identification of MBPs proved unsatisfactory. The velocities of Ca II K MBPs were instead determined using the local correlation tracking (LCT) technique (Matloch et al. 2010). This was utilized along with manual tracking to ensure accurate velocity estimates. As shown in the *G*-band analysis of Keys et al. (2011), the LCT technique produces very similar results to the automated tracking algorithm.

The ambiguity associated with their boundaries did not allow a one-to-one correspondence between all the MBPs in the *G* band and in Ca II K. Approximately 100 MBPs were analysed in Ca II K with half of them having unambiguous *G*-band counterparts. The velocity and area of each MBP were subsequently evaluated. As mentioned previously, the actual value for the area of an MBP in Ca II K can be difficult to determine due to the ambiguity of the MBP boundaries. The error in the determination of the MBP surface area was established through the calculation of mean absolute measurement errors and found to be approximately  $\pm 23 \text{ per cent}$ . Difficulties in defining an accurate area for Ca II K MBPs can be clearly seen in Fig. 1(b).

Our sample of 100 Ca II K MBPs revealed an average velocity of  $1.4 \text{ km s}^{-1}$ , with an estimated average area of  $52\,000 \text{ km}^2$ . The area of Ca II K MBPs follows a log-normal distribution similar to the *G*-band (Crockett et al. 2010), with the Ca II K area distribution shifted to higher values with a broader peak (Fig. 3 a). Velocity distributions for the observed and simulated *G*-band data sets and Ca II K are shown in Fig. 3(b). The transverse velocities of Ca II K MBPs are enhanced compared to the *G*-band (an average of  $1 \text{ km s}^{-1}$  for 6236 MBPs), with the mean absolute measurement error in both velocity values estimated to be  $0.5 \text{ km s}^{-1}$ . Their size also appear to be larger by about 63 per cent. The distributions were analysed in more detail by selecting 50 Ca II K MBPs and their corresponding

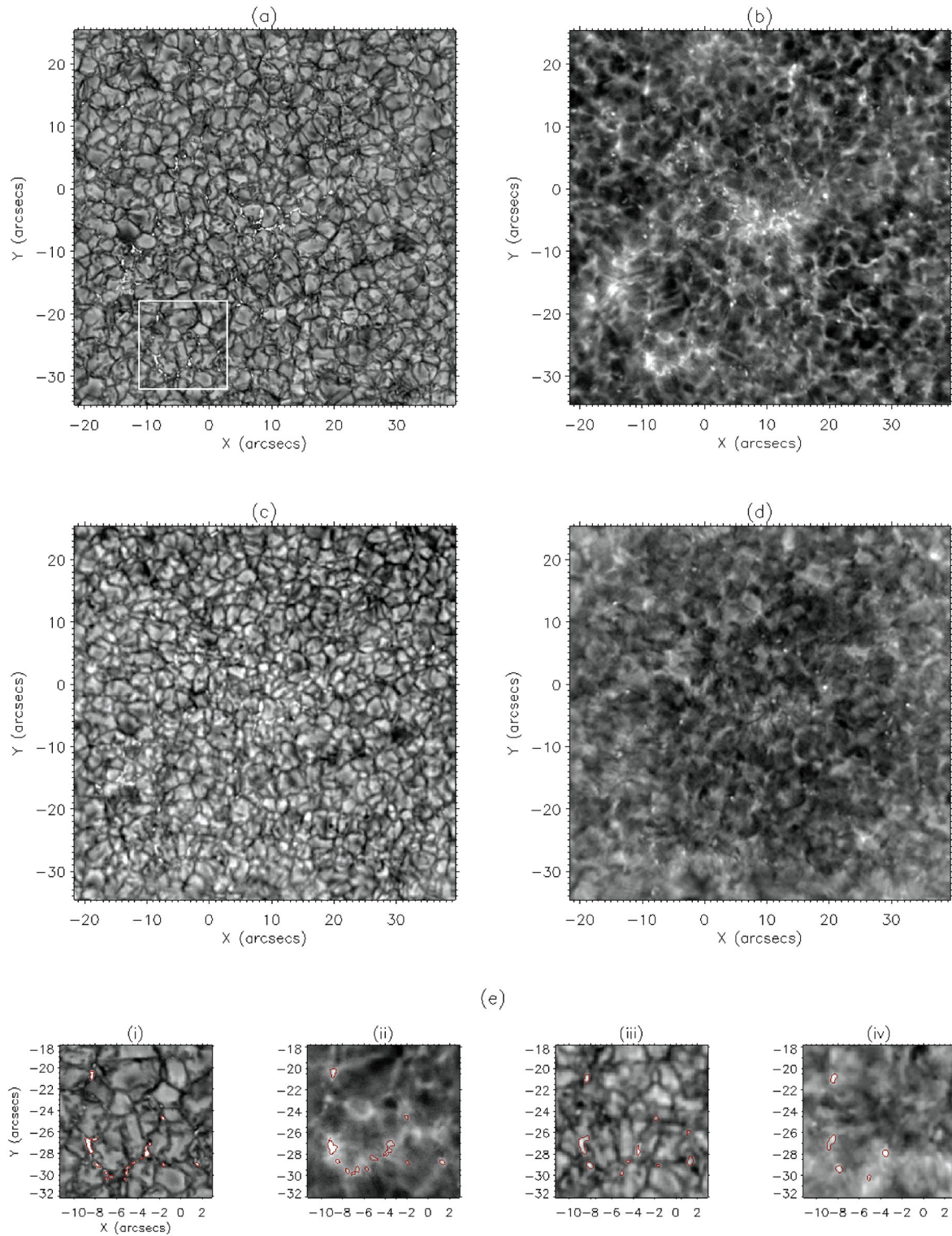


**Figure 1.** Sample ROSA and IBIS data employed in this study. (a) *G*-band image. (b) Co-spatial and co-temporal image in Ca II K. (c) and (d) Co-spatial IBIS images in the wing and the core of the Na I D<sub>1</sub> line, respectively. MBPs are abundant in (a). However, higher in the atmosphere their boundaries become more ambiguous due to reverse granulation. (e) An expanded view of the four data sets in the region outlined by the white box in (a). (i), (ii), (iii) and (iv) show expanded regions in the *G*-band, Ca II K and the wing and core of the Na I D<sub>1</sub> line, respectively. A small sample of MBPs is contoured red in the four data sets showing both groups of MBPs and isolated MBPs. The different numbers and sizes of MBPs are evident across the four data sets.



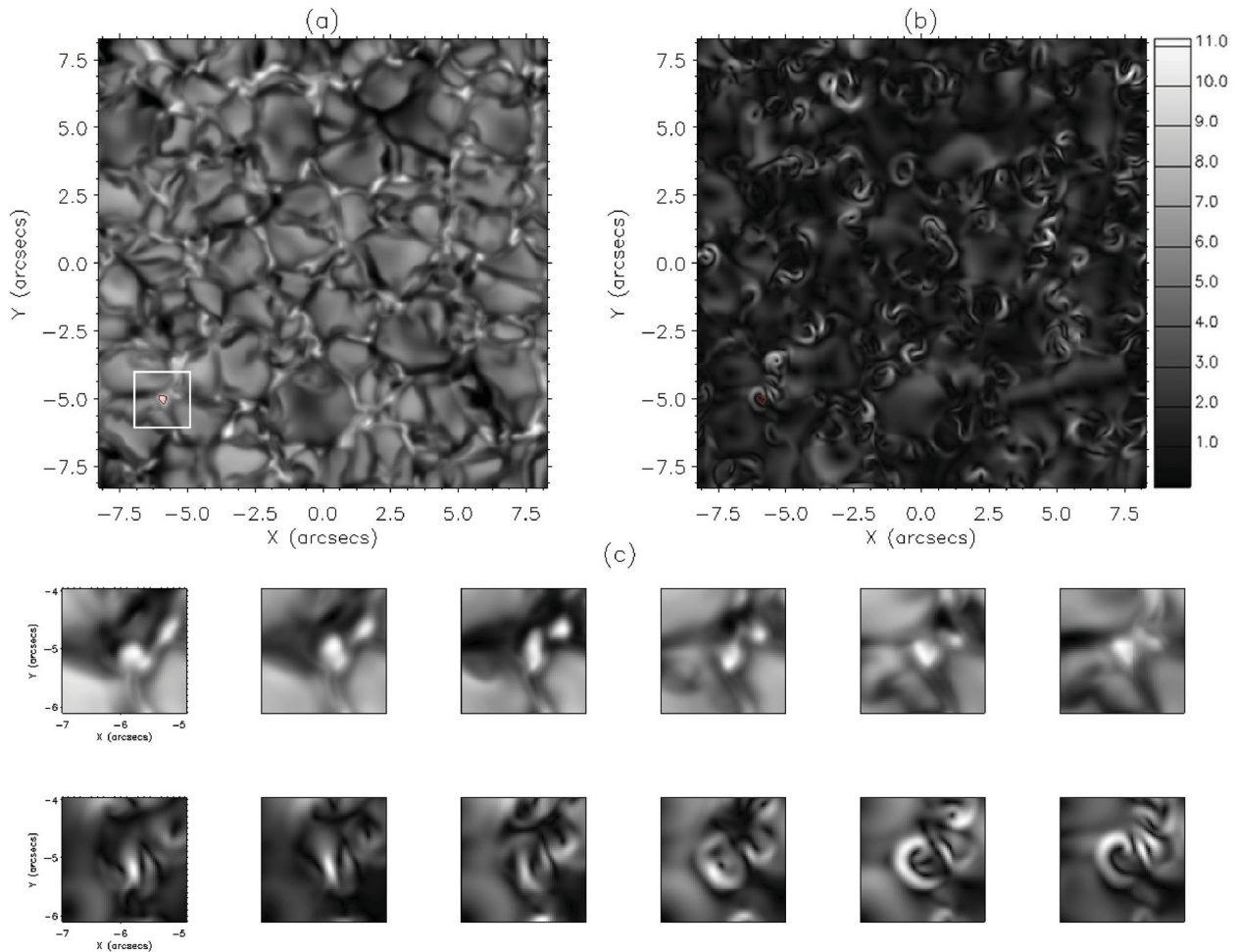


**Figure 2.** Sample images from the simulated data sets. (a) Snapshot of a  $12 \times 12$  Mm  $G$ -band simulation. (b) The corresponding velocity domain 500 km above the continuum formation layer for the image shown in (a). Velocity scale is in  $\text{km s}^{-1}$ . A sample, isolated MBP, is contoured red in (a) and (b). (c) A set of expanded panels depicting the evolution of an MBP found in the white box in (a). The top row shows the  $G$ -band images of the MBP advancing in time by  $\sim 44$  s between each panel from left to right. The bottom row shows the corresponding velocity domain images for the MBP. The final panel shows the MBP as seen in (a) and (b).

$G$ -band counterparts. Again, the average transverse velocities are  $1.8$  and  $0.8 \text{ km s}^{-1}$  in the  $\text{Ca II K}$  and  $G$ -band, respectively. The corresponding average sizes are  $51\,800$  and  $31\,300 \text{ km}^2$ . This shows a 65 per cent increase in the size of the MBPs as they extend upwards, in agreement with Jess et al. (2010a), who found an expansion of  $\sim 70$  per cent in their study of MBPs manifesting in the  $\text{Na I D}_1$  line core. Of these 50 MBPs,  $\sim 80$  per cent are isolated and the remainder are groups of MBPs. On closer inspection, the isolated MBPs have higher average velocities in both  $G$ -band and  $\text{Ca II K}$  ( $0.8$  and  $1.9 \text{ km s}^{-1}$ , respectively) compared to the groups of MBPs ( $0.6$  and  $0.3 \text{ km s}^{-1}$  in the  $G$ -band and  $\text{Ca II K}$ , respectively). As is expected, MBPs found in a group have a larger average area in both  $G$ -band and  $\text{Ca II K}$  compared to isolated MBPs. Also, the change in area between the  $G$ -band and  $\text{Ca II K}$  is more significant for isolated MBPs ( $\sim 57$  per cent change for MBP groups whereas nearly twice as large on average for isolated MBPs). This is likely the result of a higher field strength found in groups of MBPs as seen in Jess et al. (2010a). The corresponding velocities for a sample of 10 of these MBPs are given in Table 1.

We have also studied the MBPs visible in the  $\text{Na I D}_1$  line. The scanning capability of IBIS allows us to study the MBPs both in the core and wings of the line, albeit at a reduced temporal resolution

of 39.7 s. This resulted in a smaller sample of 50 MBPs present in both the wing and line core (Figs 1 c and d). The average velocity for the core of the  $\text{Na I D}_1$  line was found to be only  $0.7 \text{ km s}^{-1}$  and the average for the 486 MBPs analysed at the wing of the line to be  $0.7 \text{ km s}^{-1}$ , with a maximum value of  $6 \text{ km s}^{-1}$ . This maximum value is close to that found for the  $G$ -band. However, there is a slight discrepancy between the other velocities established for  $\text{Ca II K}$ ,  $G$ -band and  $\text{Na I D}_1$ . This is probably a result of the combination of a smaller sample size and the lower temporal resolution of the  $\text{Na I D}_1$  data sets. The errors in the velocity values in the core and the wing of the  $\text{Na I D}_1$  line are estimated to be  $0.6$  and  $0.7 \text{ km s}^{-1}$ , respectively.

The observational results were compared with radiative MHD simulations produced with the MURAM code. These simulations are described in Jess et al. (2012b) and have a cadence of  $\approx 2.1$  s. We have 724  $G$ -band MBPs in these 200 G simulated images, which have an average velocity of  $1.3 \text{ km s}^{-1}$ , a maximum velocity of  $6.9 \text{ km s}^{-1}$  and a mean lifetime of 110 s. The simulated MBP velocities have an error of approximately  $0.5 \text{ km s}^{-1}$ . A summary of results from the observed and simulated data sets is given in Table 2.

The MURAM simulations also allow us to study the corresponding velocity field at a height of 500 km above the continuum formation

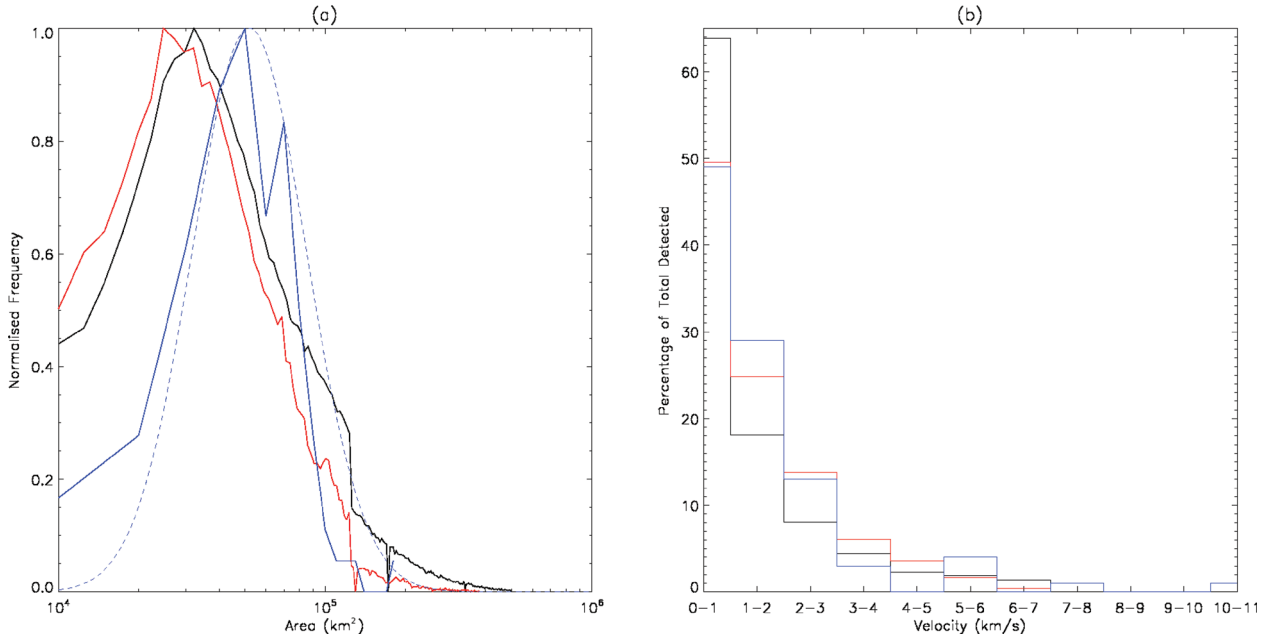


**Figure 3.** The area and velocity distributions of the observed and simulated data sets. (a) The normalized area distributions of the data sets; the *black* line shows the observed *G*-band, the *red* line the simulated *G*-band and the *blue* line the Ca II K data. The log-normal distribution of the two *G*-band data sets is clear. However, the smaller number of data points in Ca II K means that this distribution is not as clear. The *dashed blue* line shows a possible ideal log-normal curve distribution for Ca II K given better count statistics. It is evident that the Ca II K MBPs have larger areas than their *G*-band counterparts. (b) A histogram of the velocity distributions for the observed *G*-band (*black*), simulated *G*-band (*red*) and Ca II K (*blue*). The *G*-band distributions are fairly similar and that for Ca II K illustrates elevated MBP velocities.

**Table 1.** Summary of MBP characteristics directly compared at various heights.

MBP no.	Ca II K Velocity (km s <sup>-1</sup> )	Ca II K Area (km <sup>2</sup> )	<i>G</i> -band Velocity (km s <sup>-1</sup> )	<i>G</i> -band Area (km <sup>2</sup> )
1	0.74	95 000	0.75	35 000
2	3.26	66 250	1.10	40 000
3	2.09	88 750	1.62	40 000
4	1.27	131 250	0.46	35 000
5	1.36	88 750	0.81	30 000
6	1.19	87 500	0.23	50 000
7	2.04	142 500	0.13	102 500
8	0.82	113 750	0.51	52 500
9	2.77	116 250	2.54	112 500
10	0.26	156 250	0.68	110 000

**Table 2.** Summary of MBP characteristics for observations (ROSA/IBIS) and simulations (MURAM).

Data set	FOV size	Av. cadence (s)	No. of MBPs	Av. velocity (km s <sup>-1</sup> )	Max. velocity (km s <sup>-1</sup> )	Av. area (km <sup>2</sup> )
<i>G</i> -band (ROSA)	70 arcsec × 70 arcsec	2.1	6236	1	7	32 000
Ca II K (ROSA)	70 arcsec × 70 arcsec	4.2	100	1.4	10.2	52 000
Na I D <sub>1</sub> (Wing-IBIS)	83 arcsec × 83 arcsec	39.7	486	0.7	6	51 200
Na I D <sub>1</sub> (Core-IBIS)	83 arcsec × 83 arcsec	39.7	50	0.7	2.4	73 500
<i>G</i> -band (MURAM)	16 arcsec × 16 arcsec	2.1	724	1.3	6.9	26 100
Velocity domain (MURAM)	16 arcsec × 16 arcsec	2.1	724	1.8	15	N/A

layer. Transverse velocities could therefore be established for each point in the data set along with an inclination angle. The velocity maps were compared to the MBPs detected in the simulated *G*-band images and used to determine an average velocity for MBPs at this height of  $1.8 \text{ km s}^{-1}$ , with a maximum value of  $15 \text{ km s}^{-1}$ .

Our simulations reproduce the measured *G*-band and  $\text{Ca II K}$  values, albeit with slightly elevated velocities when compared to the observations. However, if we were to consider only the 50 unambiguous MBPs identified in both bandpasses, we can see that the velocities for MBPs found to be higher in the atmosphere are the same. The simulated images are from a formation height of approximately 500 km whereas Beebe & Johnson (1969) state that  $\text{Ca II K}$  is formed at a height less than 1300 km. Also, the presence of reverse granulation (as displayed in Fig. 1) would suggest that the dominant contribution to the  $\text{Ca II K}$  filter comes from the upper photosphere/lower chromosphere. A review by Rutten (2007) highlights the complexity of determining line formation regions from narrow bandpass filters and suggests that  $\text{Ca II K}$  is formed at the lower chromospheric level. Although the simulated images do not have a formation height which is explicitly the same as the observed  $\text{Ca II K}$  core images, we think that a comparison can still be made. The relatively broad bandpass of the  $\text{Ca II K}$  filter makes it difficult to assign a specific height of formation. However, there is a slight discrepancy between the values found at the formation height of the *G*-band, with the velocities of the observed data having an average of  $0.7 \text{ km s}^{-1}$  compared to  $1.3 \text{ km s}^{-1}$  in the simulated images. This is possibly due to the far superior sample size used to ascertain this value in the simulated images. Both the simulated and observed data sets show that the average velocities of MBPs increase with height. This is probably a direct consequence of the conservation of momentum combined with a decrease in the density. However, it has been shown (Jess et al. 2010a) that the expansion of flux tubes as they extend upwards is affected by the field strength of the tube. Higher field strengths lead to less expansion of the flux tube at higher levels. This could also affect the velocities of the MBPs, but more studies would be required to ascertain what effect the field strength has, if any, on the estimated velocities.

To understand the nature of these flux tubes, and how they transfer energy to higher levels, we look for changes in the velocities of MBPs between different levels as a function of time, which may indicate how rigid these flux tubes are. This study was first performed on the simulations as they contained the velocity information for higher layers, making the analysis easier. From this analysis, an average delay of  $\sim 4 \text{ s}$  was found between the *G*-band simulations and a height of 500 km above the continuum formation layer where the velocity domain is taken. This may indicate that the flux tubes between the layers are not rigid. However, as the spread of values for the delays in velocity ranges from  $\sim 2$  to  $8 \text{ s}$ , it suggests that the rigidity of these magnetic flux tubes can vary. Both the field strength and geometry of the individual tube can play a role in its flexibility.

The average magnetic field strength of *G*-band MBPs in the simulations at the continuum formation level is about 950 G, while that of the corresponding MBPs detected at 500 km above the continuum formation layer is 450 G. For the MBPs studied, the magnetic field strength is therefore reduced by  $\sim 50$  per cent between the *G*-band images and the height in the atmosphere where we take the velocity measurements. Over the same range the density is reduced by approximately a factor of 10.

The short time delays in the simulated images at the continuum formation layer and a height of 500 km would imply that energy between the two layers is transported at a very high rate. Given

that the sound and Alfvén speeds are in the ranges 11–12 and 10–15  $\text{km s}^{-1}$ , respectively, between the two layers, it seems unlikely that the observed delay is due to the movement of the footpoints in the simulation. A more likely scenario may be that the delays are produced by oblique granular shock waves, as reported by Vitas et al. (2011).

A similar analysis was performed on the observed *G*-band and  $\text{Ca II K}$  data sets. The observations show an average delay of 29 s in the response of the velocity changes between the bandpasses, with the actual values ranging between 21 and 42 s.

Due to its broad bandpass, the  $\text{Ca II K}$  filter encompasses radiation from both the chromospheric emission core and photospheric absorption profile. It is therefore extremely difficult to assign a specific height from which this radiation originates. However, the reverse granulation present in the  $\text{Ca II K}$  images indicates that emission from the upper photosphere may dominate this bandpass. A rough estimate for the distance between the *G*-band and  $\text{Ca II K}$  emission region is around 500 km. Given a delay of 29 s, a velocity of propagation of  $\sim 17 \text{ km s}^{-1}$  between the two positions for the flux tubes is suggested. This would further suggest that the propagation velocity is close to the sound speed, given typical values for the two positions. The fact that the propagation speeds are slower in the observations suggests that the physical reason behind the delay may not be the result of granular shock waves. It is possible that the delay between the *G*-band and  $\text{Ca II K}$  observations is the result of two interwoven factors: the decrease in density and the expansion of the flux tube with height. The first factor is easily explained. With a decrease in the density of the surrounding material, the flux tube is less confined and therefore less responsive to the granular movements at the photospheric level, thus resulting in delays of velocity shifts. The second factor, which as stated previously is most likely a result of the decrease in density with height, probably has an added effect on the flexibility of the tubes. As the tube expands in the atmosphere, the magnetic flux contained within is less densely held in the tube and as a result it is less rigid. This may explain the difference in delays seen in the ROSA images. Unfortunately, we do not have magnetic field information for both *G*-band and  $\text{Ca II K}$  to assess how the field strength varies with height in the observations and to investigate if there is any correlation between this and the delays in velocity shifts.

#### 4 CONCLUSIONS

We study the properties of MBPs as a function of height in the lower solar atmosphere using high-resolution multiwavelength imaging and radiative MHD simulations. The results show that the transverse velocity and area coverage of MBPs increase with height. Velocities of  $1 \text{ km s}^{-1}$  are observed for MBPs found in the *G*-band images, with the corresponding  $\text{Ca II K}$  images yielding an average velocity of  $1.4 \text{ km s}^{-1}$ . The areas of the MBPs show an average increase of approximately 63 per cent from the photosphere to the chromosphere.

Radiative MHD simulations reveal similar findings but the theoretical values are slightly elevated when compared to the observations. Due to difficulties associated with simulating the radiative emission in  $\text{Ca II K}$ , we are unable to calculate changes in the area and velocity of MBPs in simulated  $\text{Ca II K}$  images. Instead, we use the simulated horizontal velocity field and find that the delay in the changes of velocity between the two layers is approximately 4 s. We speculate that this delay may be attributed to horizontally propagating oblique granular shock waves.

The observations indicate an average delay of 29 s between the G-band and Ca II K. We surmise that the difference between the observations and the simulations is due to the height of formation of Ca II K, although the relatively broad bandpass of the Ca II K filter makes this height difficult to ascertain. It should also be noted that the difference in properties of MBPs in the observations and the simulations could be due to the different nature of turbulence conditions in the Sun and in the simulations, where the Reynolds number is very low. This is likely to affect the interaction of the flux tubes and convection at different altitudes. We have presented one of the larger scale studies of the properties of MBPs at multiple heights. The results show that the transverse velocity of MBPs increases with height, most likely as a result of the decreasing density at higher levels and the conservation of momentum.

## ACKNOWLEDGMENTS

This work has been supported by the UK Science and Technology Facilities Council (STFC). Observations were obtained at the National Solar Observatory, operated by the Association of Universities for Research in Astronomy, Inc. (AURA), under cooperative agreement with the National Science Foundation. PHK thanks the Northern Ireland Department for Employment and Learning for a PhD studentship. DBJ thanks the STFC for the award of a Post-Doctoral Fellowship. This work is based on efforts sponsored by the Air Force Office of Scientific Research, Air Force Material Command, USAF under grant number FA8655-09-13085.

## REFERENCES

- Asgari-Targhi M., van Ballegoijen A. A., 2012, *ApJ*, 746, 81  
 Beebe H. A., Johnson H. R., 1969, *Sol. Phys.*, 10, 79  
 Bonet J. A., Márquez I., Sánchez Almeida J., Cabello I., Domingo V., 2008, *ApJ*, 687, L131  
 Cauzzi G. et al., 2008, *A&A*, 480, 515  
 Cavallini F., 2006, *Sol. Phys.*, 236, 415  
 Crockett P. J., Mathioudakis M., Jess D. B., Shelyag S., Keenan F. P., Christian D. J., 2010, *ApJ*, 722, L188  
 de Wijn A. G., Stenflo J. O., Solanki S. K., Tsuentz S., 2009, *Space Sci. Rev.*, 144, 275  
 Dunn R. B., Zirker J. B., 1973, *Sol. Phys.*, 33, 281  
 Jess D. B., Mathioudakis M., Crockett P. J., Keenan F. P., 2008, *ApJ*, 688, L119  
 Jess D. B., Mathioudakis M., Christian D. J., Crockett P. J., Keenan F. P., 2010a, *ApJ*, 719, L134  
 Jess D. B., Mathioudakis M., Christian D. J., Keenan F. P., Ryans R. S. I., Crockett P. J., 2010b, *Sol. Phys.*, 261, 363  
 Jess D. B., Shelyag S., Mathioudakis M., Keys P. H., Christian D. J., Keenan F. P., 2012a, *ApJ*, 746, 183  
 Jess D. B., Pascoe D. J., Christian D. J., Mathioudakis M., Keys P. H., Keenan F. P., 2012b, *ApJ*, 744, L5  
 Keys P. H., Mathioudakis M., Jess D. B., Shelyag S., Crockett P. J., Christian D. J., Keenan F. P., 2011, *ApJ*, 740, L40  
 Langhans K., Schmidt W., Tritschler A., 2002, *A&A*, 394, 1069  
 Matloch L., Cameron R., Shelyag S., Schmitt D., Schüssler M., 2010, *A&A*, 519, A52  
 Rutten R. J., 2007, *Phys. Chromospheric Plasmas*, 368, 27  
 Sánchez Almeida J., Márquez I., Bonet J. A., Domínguez Cerdeña I., Muller R., 2004, *ApJ*, 609, L91  
 Shelyag S., Schüssler M., Solanki S. K., Berdyugina S. V., Vögler A., 2004, *A&A*, 427, 335  
 Shelyag S., Keys P. H., Mathioudakis M., Keenan F. P., 2011a, *A&A*, 526, A5  
 Shelyag S., Fedun V., Keenan F. P., Erdélyi R., Mathioudakis M., 2011b, *Ann. Geophys.*, 29, 883  
 Shelyag S., Mathioudakis M., Keenan F. P., 2012, *ApJ*, 753, L22  
 Solanki S. K., 1993, *Space Sci. Rev.*, 63, 1  
 Steiner O., Hauschildt P. H., Bruls J., 2001, *A&A*, 372, L13  
 Stenflo J. O., 1985, *Sol. Phys.*, 100, 189  
 Ulmschneider P., Zaehring K., Musielak Z. E., 1991, *A&A*, 241, 625  
 Van Ballegoijen A. A., Asgari-Targui M., Cranmer S. R., DeLuca E. E., 2011, *ApJ*, 736, 3  
 Vitas N., Fischer C. E., Vögler A., Keller C. U., 2011, *A&A*, 532, A110  
 Vögler A., Shelyag S., Schüssler M., Cattaneo F., Emonet T., Linde T., 2005, *A&A*, 429, 335  
 Wöger F., von der Lühe O., Reardon K., 2008, *A&A*, 488, 375

This paper has been typeset from a  $\text{\TeX}/\text{\LaTeX}$  file prepared by the author.